Solution for the coupled heat and mass transfer in falling film absorption using partial discretization via orthogonal collocation

Eike Cramer, Rafif S. Ramadhan, Thomas Meyer

PII: S0263-8762(25)00630-6
DOI: https://doi.org/10.1016/j.cherd.2025.11.031
Reference: CHERD 7149

To appear in: *Chemical Engineering Research and Design*

Received date : 22 August 2025
Revised date : 11 November 2025
Accepted date : 20 November 2025

Please cite this article as: E. Cramer, R.S. Ramadhan and T. Meyer, Solution for the coupled heat and mass transfer in falling film absorption using partial discretization via orthogonal collocation. *Chemical Engineering Research and Design* (2025), doi: https://doi.org/10.1016/j.cherd.2025.11.031.

Solution for the Coupled Heat and Mass Transfer in Falling Film Absorption using Partial Discretization via Orthogonal Collocation

Eike Cramer[a,b,*], Rafif S. Ramadhan[b,c], Thomas Meyer[d]

[a] *University College London, Department of Chemical Engineering, London WC1E 7JE, United Kingdom*
[b] *RWTH Aachen University, Process Systems Engineering (AVT.SVT), Aachen 52074, Germany*
[c] *Davidson School of Chemical Engineering, Purdue University, West Lafayette, IN, USA*
[d] *Technische Universität Berlin, Heat Transfer and Heat Conversion, Berlin 10587, Germany*

Abstract

Falling films are a key technology for highly exothermic absorption with high absorption or reaction heats. The textbook literature on falling films is typically limited to either the concentration or the temperature profiles, thereby ignoring the effects of one on the other. The literature on the coupled heat and mass transfer in falling films often relies on significant assumptions and simplifications to solve the coupled system of partial differential equations (PDEs). We derive a numerical scheme using orthogonal collocation on finite elements (OCFE) to solve the PDE system efficiently. The polynomial approximation in the OCFE scheme enables the accurate representation of gradients at the film interface, allowing us to compute accurate absorption rates even for short film lengths. We investigate cases of physical absorption with flow profiles and reactive absorption in comparison to a baseline flux

---

[*] Corresponding author (e.cramer@ucl.ac.uk)

balance model. Our results generally show increased absorption rates for both cases and a typical film flow length. However, a key novel insight from this work is that the absorption rate for very short film flow lengths with reactive absorption is reduced in the case of high heat of reaction.

Keywords: Falling film absorption, coupled partial differential equation system, Modelica, orthogonal collocation on finite elements, chemical falling film reactors

---

1. Introduction

Sizing a falling film apparatus remains a challenging task as the absorption rates are typically difficult to estimate and often require extensive experimentation. Mathematical models of the falling film can help reduce the number of necessary experiments and provide valuable information about the film's behavior. Such models are often based on partial differential equation (PDE) systems that describe the transport phenomena both into the film and along the film flow. In particular, in the field of absorption heat pumps, non-isothermal vapor absorption plays a significant role and has been investigated thoroughly both analytically and numerically.

A critical review of existing models has been provided by [1], stating that most models applied in physical absorption have only considered isothermal or adiabatic thermal boundary conditions. A first fully analytical solution was presented by [2] for a uniform film velocity profile. [3] applied numerical methods to solve the combined heat and mass transfer model, applying a steady-state parabolic film velocity profile. These pioneering works have been followed by several varying modeling approaches taking into account more physical aspects in non-isothermal falling film absorption. For instance, [4] and [5] introduced unidirectional diffusion in the falling film and solved the problem analytically for both isothermal and non-isothermal conditions. Nevertheless, due to mathematical restrictions of fully analytical solutions for the combined heat and mass transfer absorption problem, several works adopted numerical solution schemes, such as finite differences. Applying numerical solution schemes allows for solving the problem with fewer simplifying assumptions, e.g., on the hydrodynamics or simply by extending the problem's spatial dimensions. [6] numerically solved the problem including the inlet hydrodynamics for horizontal and vertical tubes. Besides his more complex numerical solution Andberg presented a simplified correlation with an average deviation of 6.5% on the concentration change. [7] included the effect of a wavy film flow to the model and observed a significant increase of absorbed mass flux compared to the smooth film flow results due to the transversal film velocity induced by the waves. However, Patnaik [7] doubts relevance for typical absorber conditions the since stable turbulent waves only occur at rather large film Reynolds numbers. In [8], deviations were reported for the comparison of the experimental data on the wavy film flow and the corresponding ranges of the film Reynolds numbers. More recently, [9] also modeled the effect of wavy films and the effect of mist flow on the absorption performance and solved the model numerically. The results of their wavy laminar model agreed well with regard to the absorbed mass flow but for the heat rejection capacity in the absorber also the laminar smooth model results seemed to fit rather well. [10] investigated a semi open absorption process with direct solar regeneration of the solution. Therefore, the model has been extended by the introduction of non-condensable gases. [10] developed a simpler numerical model and compared his results to [6] more complex simulation with excellent agreement. Based on experimental results, Yang presented correlations for the overall heat transfer and mass transfer coefficient with good agreement for aqueous lithium chloride as absorbent and air as non-condensable gas. Recently [11] developed a semi-empirical model for the vapor absorption in the presence of air or hydrogen, finding reasonable agreement between the correlation and the experimental data from [10]. A rather comprehensive and systematic study was presented by [12] who studied the problem in 1-D and 2-D in dimensionless form investigating the influence of various dimensionless quantities such as Peclet, Biot and Reynolds numbers. Additionally, a high-speed camera has been adopted to experimentally investigate the influence of the droplet formation and impingement on the hydrodynamics of the film in a horizontal shell and tube absorber. A recent study on the effects of droplet formation from [13] used Computational Fluid Dynamics software, volume of fluid appoach to model the two phase flow and an reasonably adapted mesh to study the impacts of droplet formation, detachment and impingement on the absorption process in detail but at reasonable computation time and effort. [14] studied the effect of varying thermophysical property data on the temperature and mass fraction profiles within the falling film, applying the finite difference method. On a system level [15] modeled the absorption chilling process for a small-scale air cooled absorption chiller working with aqueous lithium bromide and compared the simulation results to own experimental data. Surprisingly, the largest deviation was found for the condenser outlet temperature while in the other heat exchangers only smaller deviations below 15% was observed. Furthermore, analytical solutions to the falling film model have been developed recently by applying the Laplace transform [16] that allows for a more realistic thermal boundary condition of a diabatic wall as compared to the usual isothermal or adiabatic thermal wall boundary conditions for analytical solution procedures. In addition to summarizing the existing analytical solution procedures, [17] presented an analytical solution applying the Laplace transform and an approximate film velocity profile based on the square root of the film velocity.

Falling film reactors in chemical industry have been modeled and solved numerically by [18] and [19] for sulfonation reactions with a considerable increase of film temperature of up to $\Delta T_{film} = 50K$ due to the heat of reaction but neglecting the heat of absorption and hence its thermal effect on the absorbed mass flow. [20] included the effect of the heat of absorption in the model for the chlorination reaction of decane. They solve the system of nonlinear PDEs by numerical integration, reporting some severe numerical difficulties considering both the temperature profile in the gas and liquid phases. By further simplifying the problem, they were able to solve the problem numerically but obtained some oscillating solutions, which they presumed to be related to the reactor itself.

In this study, we also consider an absorbing falling film in which a chemical reaction occurs depending on the concentration of the absorbate. We consider the heat of absorption as well as the heat of reaction in the model and solve the nonlinear PDE system numerically to investigate the thermal effect on vapor absorption in liquid films in chemical falling film reactors, discussing the obtained reaction rates and steady states. The models present systems of coupled PDEs, meaning that the solutions of the PDEs influence each other. We present a numerical solution scheme for the coupled PDE system using partial discretization via orthogonal collocation on finite elements (OCFE) [21, 22]. OCFE has proven to be an efficient and accurate approximation of dynamical systems and is commonly used to solve nonlinear differential equations in chemical engineering [21, 23]. Using OCFE, as opposed to other numerical schemes, allows us to use highly descriptive approximations like orthogonal polynomials while maintaining efficient computations. For falling film absorption, an accurate description of the gradients is critical to solving the coupling equations and to computing the absorption rates, i.e., the most important variable for absorber sizing. OCFE brings the particular advantage that the approximation in film thickness direction via polynomials yields an efficient and highly accurate option for computing gradients of the profiles at the film interface. For OCFE, we first split the film thickness coordinate into finite elements of variable size. In each finite element, we approximate the temperature and concentration profiles using polynomials, specifically the orthogonal Hermite polynomials. Through the OCFE approximation, we obtain a reformulation of the PDE to a differential algebraic equation system (DAE), which can be solved efficiently using widely available solvers. Furthermore, using orthogonal polynomials yields an improved approximation, particularly for high gradients as are observed at the film interface and short flow length values. We implement the resulting DAE using the object-oriented modeling language *Modelica* and solve the program in *Dymola*. We opt for the implementation in *Modelica* to make use of its object oriented programming structure allowing us to reuse a generic PDE discretization for both the temperature and the concentration profils. Furthermore, *Dymola* provides powerful DAE solvers to efficiently solve the resulting DAE system. We validate our OCFE scheme via a comparison to the analytical solution in our previous work [24].

Our numerical solution scheme reproduces the results of our analytical solution reported in [24], validating the numerical scheme. Furthermore, we investigate two further falling film absorption models. The first model proposed by [3] includes the laminar film profile in the formulation, and we derive the second model, which includes reactive absorption with a first-order reaction. The second model is a first order non-isothermal reaction model that uses the same modeling assumptions as our baseline model in [24], except for the reaction which adds terms in both the concentration and temperature equation. We opt for this isolated analysis of the first-order non-isothermal reaction to allow for unbiased evaluations without overlapping effects resulting from multiple phenomena. The results for the baseline model from [24] and the solution to the laminar film model by [3] confirm previous results from the literature. However, our simulation of the reactive absorption with highly exothermic reactions reveals a reduction of the absorption rates for short flow lengths, which has previously not been observed.

The remainder of this work is organized as follows: Section 2 presents the falling film models, including cases with laminar film profiles and first-order reactions. Furthermore, the section presents the dimensionless form of all models. In Section 3, we present our numerical solution scheme via partial discretization using OCFE. Section 4 validates the numerical scheme by comparison to the analytical solution in [24] and presents the results of the numerical solutions to the models discussed in Section 2. Finally, Section 5 highlights the most important insights and, thereby, concludes this work.

2. Falling film absorption models

Section 2.1 reviews the baseline baseline flux balance model from our previous work in [24] and [16], where the analytical solution will be used to validate the numerical scheme introduced in Section 3. Next, Section 2.2 and Section 2.3 introduce models for the stationary laminar flow model and the first-order reaction model, respectively. Finally, Section 2.4 shows the dimensionless generalization of all three models and the boundary conditions.

2.1. Baseline diffusion convection model

The baseline model for this work is the flux balance model obtained from our previous works in [24] and [16]. Here, we derived a generic differential two-dimensional flux balance equation for the falling film in steady-state:

$$0 = -\frac{\partial j}{\partial x} - \frac{\partial j}{\partial y} \tag{1}$$

Here, j are the fluxes of the respective conservation quantity, x is the direction of flow of the film, and y is the transverse direction. Hence, Equation (1) describes the conservation law for any conservation quantity in a two-dimensional differential volume at steady state. For this baseline model, we assume a frictionless flow, i.e., a constant film velocity $\bar{u}$, only convective transport in the flow direction x, and only diffusive transport in the transverse direction y. Furthermore, we neglect the effects of unidirectional diffusion and assume a constant film thickness. For a discussion of these effects, we refer the interested reader to [4].

Introducing the mass transport terms into Equation (1), we obtain the following expression for the absorbate balance equation:

$$\bar{u}\frac{\partial c}{\partial x} = D\frac{\partial^2 c}{\partial y^2} \tag{2}$$

Here, c is the absorbate mass fraction and D is the diffusion coefficient. The energy balance reads:

$$\bar{u}\frac{\partial T}{\partial x} = \alpha\frac{\partial^2 T}{\partial y^2} \tag{3}$$

Here, α is the thermal diffusivity. The model is called the convection diffusion model, as it considers only convection in the film flow direction and only diffusion in the transverse direction. For details on how to derive the balance equations, please refer to the original publications [24, 16].

In 1977, [2] proposed an approximation of the thermodynamic coupling of the temperature and the concentration profile at the film interface. The approximation assumes a linear relationship between the interface temperature $T(x, y = 0) = T_I(x)$ and the interface concentration $c(x, y = 0) = c_I(x)$:

$$T_I(x) = A - Bc_I(x) \tag{4}$$

Here, the subscript I indicates the interface with $y = 0$. Both the interface temperature T_I and concentration c_I are functions of the flow length x. This linear approximation has later been used by [3], [4], and [24]. This linear relation for the thermodynamic equilibrium condition is indispensable for solving the problem analytically and hence is a deliberate simplification here. Nevertheless, in [25] we compared this simplification of the linear profile to actual equilibrium data of aqueous lithium bromide solution based on experimental data from [26]. The analysis revealed that the deviation due to this linearization is reasonably small as long as the mass fraction differences between bulk and interface are below $\Delta c < 0.1$.

The interface gradients of temperature and mass fraction are interconnected through an interface energy balance that considers latent heat. The heat of absorption is influenced by the mass fraction gradient at the interface and must be carried into the bulk film flow via heat conduction, which is dependent on the temperature gradient at the interface. Thus, the second coupling condition at the interface is given by:

$$\dot{q}_{abs}(x) = \dot{m}_{abs}(x)\Delta h_A \tag{5}$$

Here, $\dot{q}_{abs}$ is the heat of absorption, and $\dot{m}_{abs}$ is the absorption mass flux. As all transport is normal to the interface, the heat gets transported into the film by conduction and the mass via diffusion. For the baseline model, this yields:

$$\lambda \frac{\partial T}{\partial y}\bigg|_I (x) = \rho D \frac{\partial c}{\partial y}\bigg|_I (x)\Delta h_A \tag{6}$$

Again, the subscript I indicates the interface with $y = 0$, and both gradients are functions of the flow length x . We set Dirichlet boundary conditions for the wall temperature:

$$T(x, y = \delta) = T_W \tag{7}$$

For the concentration, there is no mass transport through the wall, which results in a Neumann boundary condition of a null gradient, as we assume only diffusive transport in the transverse direction:

$$\frac{\partial c}{\partial y}\bigg|_W (x) = 0 \tag{8}$$

Here, the subscript W indicates the wall with $y = \delta$.

At the inlet, we assume the film to be ideally mixed with constant concentration and temperature for all y:

$$c(x = 0, y) = c_0 \tag{9}$$

$$T(x = 0, y) = T_0 \tag{10}$$

2.2. Laminar flow profile

The presented laminar flow model is equivalent to [3]. This laminar flow model extends the baseline model to consider a steady-state laminar flow profile of a falling film. The flow is fully developed, and only wall shear forces are exerted on the film. There is no shear stress at the film surface from the vapor side. The velocity profile, as derived in [27], reads:

$$u_x(y) = \frac{\rho g \delta^2}{2\mu}\left[1 - \left(\frac{y}{\delta}\right)^2\right] = u_{max}\left[1 - \left(\frac{y}{\delta}\right)^2\right] \tag{11}$$

Figure 1 shows a sketch of the laminar film velocity profile.

The velocity profile can also be expressed in terms of the average velocity $\bar{u}_x$. First, we integrate Equation (11) over the film thickness to obtain an expression for the average velocity:

$$\bar{u}_x = \frac{1}{\delta}\int_0^\delta u_x \, dy = \frac{2}{3}u_{x,max} \tag{12}$$

Then, we can enter Equation (12) into Equation (11):

$$u_x(y) = \frac{3}{2}\bar{u}_x\left[1 - \left(\frac{y}{\delta}\right)^2\right] \tag{13}$$

Analogous to Section 2.1, the governing PDEs can be derived from the mass and energy balance of an infinitely small film element as presented in

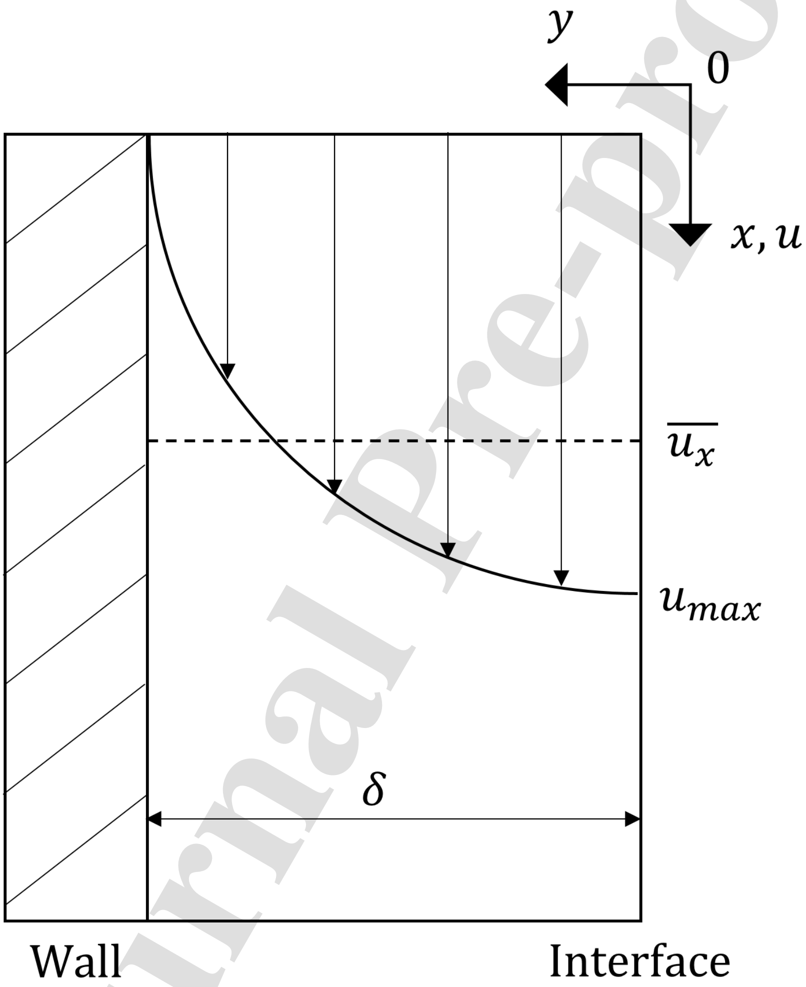

Figure 1: Steady-state flow profile of a falling film, see Equation (11).

[24]. Assuming a fully established flow, the absorbate mass balance and energy balance are obtained as follows [3]:

$$u_x(y)\frac{\partial c}{\partial x} = D\frac{\partial^2 c}{\partial y^2}, \tag{14}$$

$$u_x(y)\frac{\partial T}{\partial x} = \alpha\frac{\partial^2 T}{\partial y^2}. \tag{15}$$

Note that we assume a fully established flow profile constant over x. Thus $u_x(y)$ can be separated from the differential term for the convective flow in x-direction. The initial and boundary conditions are the same as those for the baseline model.

2.3. First order non-isothermal reaction

As an additional consideration, we model a diffusion-convection-reaction model for reactive absorption with a first-order non-isothermal reaction. We conduct an isolated investigation of the effects of the non-isothermal reaction to gain insights without overlapping effects from other phenomena. Thus, the first-order non-isothermal reaction model is the baseline flux balance model with a first-order reaction term.

We model a simple first-order reaction with the reaction rate given by:

$$\dot{r} = -kc\rho \tag{16}$$

The reaction heat is described through a constant reaction enthalpy:

$$\dot{q} = \dot{r}\Delta h_R \tag{17}$$

Adding the reaction term to the baseline model results in:

$$\bar{u}\frac{\partial c}{\partial x} = D\frac{\partial^2 c}{\partial y^2} - kc \tag{18}$$

$$\bar{u}\frac{\partial T}{\partial x} = \alpha\frac{\partial^2 T}{\partial y^2} + kc\frac{\Delta h_R}{c_P} \tag{19}$$

Table 1: Definition of dimensionless numbers.

Name	Symbol	Definition
Damköhler	Da	$\frac{k\delta^2}{D}$
Lewis	Le	$\frac{\alpha}{D}$
Stefan absorption	$\widetilde{St}_A$	$\frac{c_p(T_{eq}-T_0)}{\Delta h_A(c_{eq}-c_0)}$
Stefan reaction	$\widetilde{St}_R$	$\frac{c_p(T_{eq}-T_0)}{\Delta h_R(c_{eq}-c_0)}$

Note that the concentration appears in Equation (19) through the reaction heat term.

The model equations in Equation (18) and (19) apply to both exothermic and endothermic reactions. For the exothermic case, the wall is cooled:

$$T_W \leq T_0, \tag{20}$$

and for the endothermic case, the wall is heated:

$$T_W \geq T_0. \tag{21}$$

In the following, we limit the analysis to the exothermic case. Furthermore, we assume constant parameters, e.g., the reaction rate constant is assumed to be independent from temperature for the sake of comparison and a consequent discussion.

2.4. Dimensionless models

We generalize our models to a dimensionless form using the dimensionless coordinates and state variables formerly used in [16]:

Dimensionless flow length: $\xi = \frac{x}{\delta}\frac{\alpha}{\bar{u}\cdot\delta} = \frac{x}{\delta}\cdot\frac{1}{Pe_\alpha}$

Dimensionless film thickness: $\eta = \frac{y}{\delta}$

Dimensionless concentration: $\gamma = \frac{c - c_0}{c_{eq} - c_0}$

Dimensionless temperature: $\theta = \frac{T - T_0}{T_{eq} - T_0}$

Here, the dimensionless film flow length ξ is of great significance for the evolution of the whole absorption and reaction process. It can be considered as sort of a thermal entrance length of the problem, since the relative flow length x/δ is divided by the thermal Peclet number. We refer to small values of ξ if $\xi < 0.1$ as long as the cooling effect of the wall does not yet affect the film's surface. Consequently, for large values if $\xi > 1$ the corresponding temperature profiles across the film are fully developed across the film and the cooled wall affects the interface thermally. Table 1 lists the dimensionless numbers.

In the following, we present the dimensionless versions of the models derived in Section 2.

Using the dimensionless numbers in Table 1, the baseline model from Section 2.1 is given by [24]:

$$\frac{\partial \theta}{\partial \xi} = \frac{\partial^2 \theta}{\partial \eta^2} \tag{22}$$

$$\frac{\partial \gamma}{\partial \xi} = \frac{1}{Le} \frac{\partial^2 \theta}{\partial \eta^2}. \tag{23}$$

For the inlet conditions $\theta(\xi = 0, \eta) = \theta_0$ and $\gamma(\xi = 0, \eta) = \gamma_0$, the definitions yield:

$$\theta_0 = \gamma_0 = 0.$$

The dimensionless wall temperature $\theta(\xi, \eta = 1) = \theta_W$ is set to:

$$\theta_W = -1,$$

for all cases. The Neumann boundary condition for the concentration gradient at the wall is:

$$\frac{\partial\gamma}{\partial\eta}(\xi,\eta=0)=\left.\frac{\partial\gamma}{\partial\eta}\right|_{W}=0 \tag{24}$$

The dimensionless coupling conditions are given by [24]:

$$1=\theta_I+\gamma_I \tag{25}$$

$$\left.\frac{\partial\gamma}{\partial\eta}\right|_{I}=Le\widetilde{St}_A\left.\frac{\partial\Theta}{\partial\eta}\right|_{I} \tag{26}$$

Here, $\theta_I=\theta(\xi,\eta=0)$ and $\gamma_I=\gamma(\xi,\eta=0)$ are the dimensionless temperature and concentration at the interface, and $\left.\frac{\partial\theta}{\partial\eta}\right|_{I}=\frac{\partial\theta}{\partial\eta}(\xi,\eta=0)$ and $\left.\frac{\partial\gamma}{\partial\eta}\right|_{I}=\frac{\partial\gamma}{\partial\eta}(\xi,\eta=0)$ are the dimensionless gradients of temperature and concentration at the interface, respectively.

The heat and mass balances of the laminar flow profile model (Section 2.2) yield the following dimensionless PDE system:

$$\frac{\partial\theta}{\partial\xi}=\frac{2/3}{1-\eta^2}\frac{\partial^2\theta}{\partial\eta^2}, \tag{27}$$

$$\frac{\partial\gamma}{\partial\xi}=\frac{2/3}{Le(1-\eta^2)}\frac{\partial^2\gamma}{\partial\eta^2}, \tag{28}$$

For the first-order reaction model (Section 2.3), the dimensionless model reads:

$$\frac{\partial\gamma}{\partial\xi}=\frac{1}{Le}\frac{\partial^2\theta}{\partial\eta^2}-\frac{Da}{Le}(\gamma-\frac{c_0}{c_{eq}-c_0}) \tag{29}$$

Here, $Da=\frac{k\delta^2}{D}$ is the Damköhler number. We assume $c_0=0$ for the first-order reaction as there is typically no absorbate in the film for reactive absorption. Thus, we obtain:

$$\frac{\partial\gamma}{\partial\xi}=\frac{1}{Le}\frac{\partial^2\gamma}{\partial\eta^2}-\frac{Da}{Le}\gamma \tag{30}$$

Table 2: Overview of considered phenomena in falling film models.

Model	Flow Profile	Non-Isothermal Reaction
Baseline Flux Balance	✗	✗
Laminar Flow	✓	✗
First-Order Non-Isothermal Reaction	✗	✓

With the same assumption, the energy balance in Equation (19) translates to:

$$\frac{\partial \theta}{\partial \xi} = \frac{\partial^2 \theta}{\partial \eta^2} + \frac{Da}{\widetilde{St}_R \; Le}\gamma. \tag{31}$$

Here, $\widetilde{St}_R$ is the modified Stefan number for the reaction, see Table 1.

As an overview, Table 2 summarizes the phenomena considered in the different models.

3. Numerical solution scheme

In our previous work in [24] and [16], we derived an analytical solution to the dimensionless baseline model. In this work, we present a numerical solution scheme that translates to other models of the falling film systems.

This section first presents a partial discretization of the PDEs using orthogonal collocation on finite elements (OCFE) in Section 3.1. Section 3.2 shows how we can use Gaussian Quadratures in a convenient combination with the orthogonal collocation to integrate over the film thickness. Finally, Section Appendix A.1 presents our implementation in the modeling language *Modelica* and solution via *Dymola*.

3.1. PDE Solution via Partial Discretization

Our numerical scheme uses OCFE [28] to discretize the film thickness coordinate η. The partial discretization translates the PDE system to a DAE system that can be solved efficiently using *Modelica* and *Dymola*. Furthermore, the finite element scheme is a flexible environment to use expressive approximations such as orthogonal polynomials. We present the discretization scheme using the dimensionless baseline temperature equation (Equation (22)) due to its simplicity. However, the approach translates to all other versions of the coupled PDE system presented in Section 2.

For OCFE, we first divide the problem domain, i.e., the film thickness $\eta \in [0,1]$, into $k = 1,\ldots,NE$ finite elements.

$$0 = \eta_1 < \eta_2 < ... < \eta_{NE} < \eta_{NE+1} = 1 \tag{32}$$

The width of the individual elements $h_k = \eta_{k+1} - \eta_k$ is flexible, and the implementation allows for variable finite element sizes. Furthermore, we introduce a local variable $z \in [0,1]$ within a finite element to represent the position in η:

$$z = \frac{\eta - \eta_k}{h_k} \tag{33}$$

We use third-order Hermite polynomials [29] to approximate the solution of the PDE in η. For each finite element, the solution is given by a third-order polynomial of z:

$$\theta_k(z,\xi) \approx \sum_{l=1}^{4} a_{k,l}(\xi)\mathcal{H}_l(z) \tag{34}$$

Here, $\mathcal{H}_l$ is the cubic Hermite basis polynomials and $a_{k,l}$ the collocation coefficients at the k-th finite element and the l-th collocation point. Note that the collocation coefficients $a_{k,l}$ are functions of the flow coordinate ξ as the system is only discretized over η. We opt for Hermite polynomials due to their lower computational cost compared to using Lagrangian interpolants [22, 29]. Furthermore, Hermite polynomials have proven advantageous for second-order differential boundary value problems. Equation (35) lists the third-order Hermite polynomials as a function of the local variable z [28].

$$\mathcal{H}_1(z, h_k) = (1-z)^2(1+2z) \tag{35a}$$

$$\mathcal{H}_2(z, h_k) = z(1-z)^2 h_k \tag{35b}$$

$$\mathcal{H}_3(z, h_k) = z^2(3-2z) \tag{35c}$$

$$\mathcal{H}_4(z, h_k) = z^2(z-1)h_k \tag{35d}$$

For details on the definition of orthogonal polynomials and Hermite polynomials, we refer to textbooks on the subject [29].

Fitting the cubic polynomials requires four collocation points, i.e., evaluation points for the polynomials [22]. In practice, we evaluate Equation (34) only at these collocation points. Hence, Equation (34) is discretized for all finite elements and all collocation points, i.e., $\forall k \in [1, NE]$, $\forall i \in [1, 4]$, respectively:

$$\theta_k(z_i, \xi) = \sum_{l=1}^{4} a_{k,l}(\xi)\mathcal{H}_l(z_i) \tag{36}$$

In practice, a clever choice of collocation points can lead to sparse equation systems, which leads to shorter solution times [23]. There is a multitude of options for selecting collocation points. In this work, we use the shifted roots of the second-order Legendre polynomial $P_2(x) = (3x^2 - 1)/2$ as interior collocation points [23]. The roots are shifted from the original interval of $[-1, 1]$ to the local coordinate system which gives us the following collocation points: $z_1 = 0$, $z_2 = \frac{3-\sqrt{3}}{6}$, $z_3 = \frac{3+\sqrt{3}}{6}$, $z_4 = 1$ [30]. In the Appendix, the values of the cubic Hermite basis polynomials at the shifted roots of the second-order Legendre polynomial are listed in Table A.4.

Expressing θ in the form given in Equation (34) trivially extends to first and second derivatives by differentiating the orthogonal polynomials. The first and second derivatives of Equation (34) are given by:

$$\frac{\partial \theta_k}{\partial z}(z, \xi) \approx \frac{1}{h_k} \sum_{l=1}^{4} a_{k,l}(\xi) \mathcal{A}_l(z) \tag{37}$$

$$\frac{\partial^2 \theta_k}{\partial z^2}(z, \xi) \approx \frac{1}{h_k^2} \sum_{l=1}^{4} a_{k,l}(\xi) \mathcal{B}_l(z) \tag{38}$$

Here, $\mathcal{A}_l$ and $\mathcal{B}_l$ are the first and second derivatives of the cubic Hermite basis polynomials, respectively. The expressions for the first and second derivatives are given in Appendix Appendix A. Again, the first and second derivatives are evaluated only at the collocation points. The value of the derivatives at the collocation points can be found in the Appendix in Table A.4. Note that the collocation coefficients $a_{k,l}$ are the same functions of ξ as the coefficients in Equation (34).

The partially discretized PDE for θ or the dimensionless baseline model is then given by:

$$\begin{aligned} \frac{\partial \theta_{k,i}}{\partial \xi} &= \frac{\partial^2 \theta_{k,i}}{\partial z^2} \\ &= \frac{1}{h_k^2} \sum_{l=1}^{4} a_{k,l}(\xi) \mathcal{B}_l(z_i) \\ &\forall k \in [1, NE],\ \forall i \in \{2, 3\} \end{aligned} \tag{39}$$

The right-hand side is the approximation via the OCFE scheme given by Equation (38). The left-hand side is the first-order derivative of θ at the

$\{k, i\}$ position w.r.t. the flow coordinate ξ:

$$\frac{\partial \theta_{k,i}}{\partial \xi} = \sum_{l=1}^{4} \frac{d a_{k,l}}{d\xi} \mathcal{H}_l(z_i) \tag{40}$$

To ensure continuity between neighboring finite elements, the solution at the boundary of two elements must be equal. A second-order PDE system also requires the continuity of the first derivative [28]. By using cubic Hermite polynomials as basis functions, the continuity constraints can be fulfilled by reusing the collocation coefficients:

$$\theta_k \overset{!}{=} \theta_{k+1} \Rightarrow a_{k,3} \overset{!}{=} a_{k+1,1} \quad \forall k \in [1, NE-1] \tag{41}$$

$$\frac{\partial \theta_k}{\partial z} \overset{!}{=} \frac{\partial \theta_{k+1}}{\partial z} \Rightarrow a_{k,4} \overset{!}{=} a_{k+1,2} \quad \forall k \in [1, NE-1] \tag{42}$$

Hence, there are $2(NE-1)$ connectivity equations to connect the NE finite elements. The resulting differential-algebraic system of equations (DAE) can be solved efficiently using DAE solvers.

We write Equation (40) only for the second and third collocation points. The differential part of the equation requires the variables on the interior collocation points to be differential variables (hatched elements in Figure 2). For the first and fourth collocation points (light grey elements in Figure 2), the values of the collocation coefficients $a_{k,l}$ are given via the boundary conditions and the connectivity conditions between the finite elements. Hence, the first and fourth elements are defined as algebraic variables.

Analogous to θ, the discretization of the dimensionless absorbate concentration γ reads:

$$\frac{1}{Le} \frac{\partial \gamma_{k,i}}{\partial \xi} = \frac{\partial^2 \gamma_{k,i}}{\partial z^2} \quad \forall k \in [1, NE],\ \forall i \in \{2, 3\} \tag{43}$$

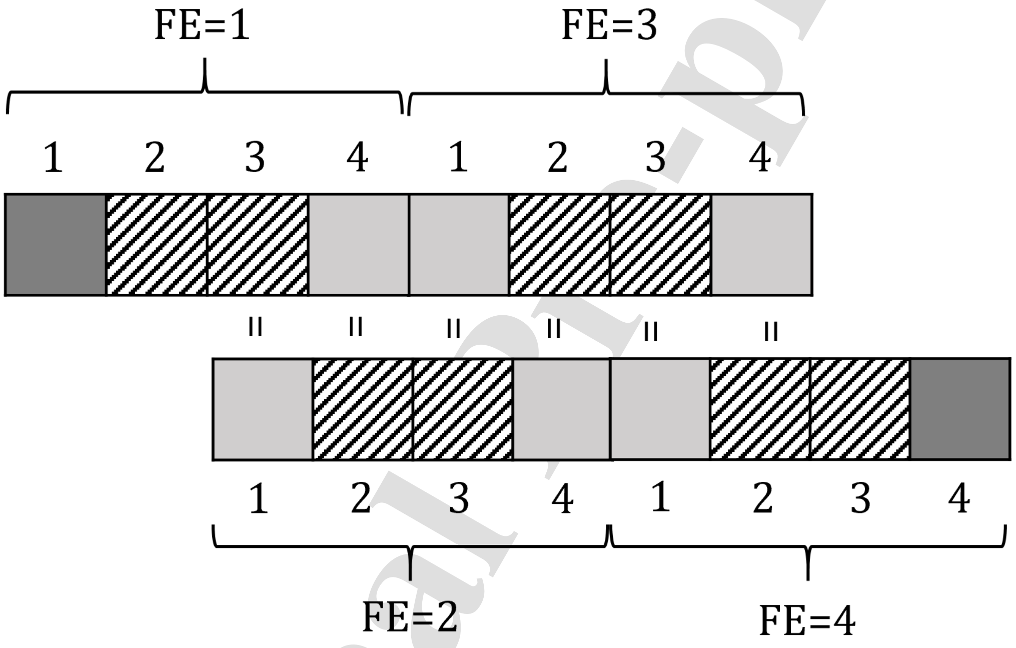

Figure 2: Finite element grid and interior collocation points. Dark grey elements are assigned via boundary conditions, and light grey via continuity constraints. The hatched elements are differential variables, and the colored elements are algebraic variables.

Similar to Equations (34), (37), and (38) the approximation of γ via the OCFE scheme is given by:

$$\gamma_k(z,\xi) \approx \sum_{l=1}^{4} b_{k,l}(\xi)\mathcal{H}_l(z) \tag{44}$$

$$\frac{\partial \gamma_k}{\partial z}(z,\xi) \approx \frac{1}{h_k}\sum_{l=1}^{4} b_{k,l}(\xi)\mathcal{A}_l(z) \tag{45}$$

$$\frac{\partial^2 \gamma_k}{\partial z^2}(z,\xi) \approx \frac{1}{h_k^2}\sum_{l=1}^{4} b_{k,l}(\xi)\mathcal{B}_l(z) \tag{46}$$

Here, $b_{k,l}(\xi)$ are the collocation coefficients for γ.

The laminar film model and first-order reaction model are discretized analog to the baseline model, i.e., Equations (34), (37), and (38) and Equations (44), (45), and (46) are inserted into the respective balance equations.

3.2. Integration over film thickness

Obtaining averages over the film thickness requires integration over η. However, we discretize the film coordinate η, and thus, there is no continuous function for $\theta(\eta)$ or $\gamma(\eta)$. Hence, there is no closed-form solution for integrals such as:

$$\int_0^1 \gamma(\xi)\, d\eta.$$

Instead of running a separate integration, we use the transformed Gauss-Legendre quadrature for numerical integration [31].

For an interval $[a,b]$, the Gauss-Legendre quadrature is defined as follows:

$$\begin{aligned}\int_a^b \gamma(\eta)\, d\eta &= \int_{-1}^{1} \gamma(\frac{h}{2}\eta + \frac{a+b}{2})\, d\eta \\ &= \frac{h}{2}\sum_{i=1}^{N} w_i \gamma(\frac{h}{2}\eta_i + \frac{a+b}{2})\end{aligned} \tag{47}$$

where $h = b - a$, N is the quadrature order, w_i is the quadrature weights, and η_i is the quadrature points.

For Gauss-Legendre quadrature, $w_i = 1$ and η_i are the roots of the N-th degree Legendre polynomials. We approximated θ and γ using third-order polynomials and, thus, $N = 2$ [31]. For our problem, the quadrature equation reads:

$$\int_0^1 \gamma(\eta)\, d\eta = \frac{1}{2}\sum_{i=1}^{2}\gamma(\frac{1}{2}\eta_i + \frac{1}{2}) \tag{48}$$

In our problem, we can divide the integral over the entire range of η into multiple integrals that correspond to the finite-element grid set through the OCFE scheme:

$$\begin{aligned}\int_0^1 \gamma(\xi)\, d\eta = &\int_{\eta_1=0}^{\eta_2} \gamma(\xi)\, d\eta \\ &+ \int_{\eta_2}^{\eta_3} \gamma(\xi)\, d\eta \\ &+ ... + \int_{\eta_{NE}}^{\eta_{NE+1}=1} \gamma(\xi)\, d\eta\end{aligned} \tag{49}$$

Then, we calculate the integrals in the sub-intervals using the Gauss-Legendre quadrature.

Note that the quadrature points are the same points as the collocation points. Thus, we can reuse the collocation structure and obtain the function values at the quadrature points, as we used the roots of second-degree Legendre polynomials as the collocation points.

3.3. Integration over film length

We need to integrate over the film length to obtain the integral properties of the film. To obtain these integrals, we add the differential form of these properties to the DAE system so that they are integrated simultaneously.

For instance, take the average interface concentration:

$$\bar{\gamma}_I = \frac{1}{\xi} \int_0^{\xi} \gamma_I \, d\xi \tag{50}$$

We can compute $\bar{\gamma}_I$ turning Equation (50) into a DAE:

$$\frac{\partial \gamma_{I,int}}{\partial \xi} = \gamma_I; \;\; \gamma_{I,int}(\xi = 0) = \gamma_{I,0} \tag{51}$$

$$\bar{\gamma}_I = \frac{1}{(\xi + \varepsilon)} \gamma_{I,int} \tag{52}$$

Here, $\gamma_{I,int}$ is a helper variable. Note that we add a small value $\varepsilon = 10^{-9}$ to ξ in the computation of $\bar{\gamma}_I$ to avoid numerical errors from dividing by $\xi = 0$.

4. Results

In this section, we present and discuss the simulation results for the different modeling cases outlined in Section 2. Table 3 lists the values of the dimensionless numbers used throughout our analysis. In a previous study on the physical absorption of water vapor in aqueous lithium bromide solutions [32], the values of the Lewis and Stefan numbers for pure physical absorption have been identified in the range of $Le = 100$ and $St_A = 0.1$. The results of this analytical solution to the baseline model model for aqueous lithium bromide have been successfully validated with experimental data from [33]. Furthermore, we analyzed the effects of different Le numbers in [24] and will not repeat this analysis to avoid redundancy. For the chemical reaction model we have varied the Damköhler and Stefan number for the reaction in a wide range since these two values depend on either the reaction rate constant k or the reaction enthalpy Δh_R.

Table 3: Values of the dimensionless number used throughout the analysis. Note that $\widetilde{St}_R \to \infty$ indicates isothermal reaction, i.e., no reaction heat.

Number	Value
Da	100, 1000, 10000
Le	100
$\widetilde{St}_A$	0.1
$\widetilde{St}_R$	0.1, 1, ∞

4.1. Validation of Numerical Results

We validate our numerical solution for the baseline model via comparison with the analytical solution presented in [24]. For this purpose, we define a general error variable ϵ:

$$\epsilon = \frac{\gamma_{analytical} - \gamma_{OCFE}}{\gamma_{ref}} \tag{53}$$

We set $\gamma_{ref} = 1$ such that the relative error is equal to the absolute numerical error. Using ϵ, we can also analyze the effect of using various grids to discretize the calculation domain. The numerical errors for $\xi = 0.02$ and $\xi = 5$ over the film coordinate η are given in Figure 3. The numerical error is small, with error values scaling in 10^{-5} at the interface and below elsewhere. For small ξ, the gradients at the interface are extremely high, which makes it difficult to approximate using numerical schemes. The error decreases for higher values of the dimensionless film length. Henceforth, we view the numerical scheme as validated and proceed to discuss the simulation results. In the following, all presented results are obtained using the numerical solution scheme presented in Section 3.

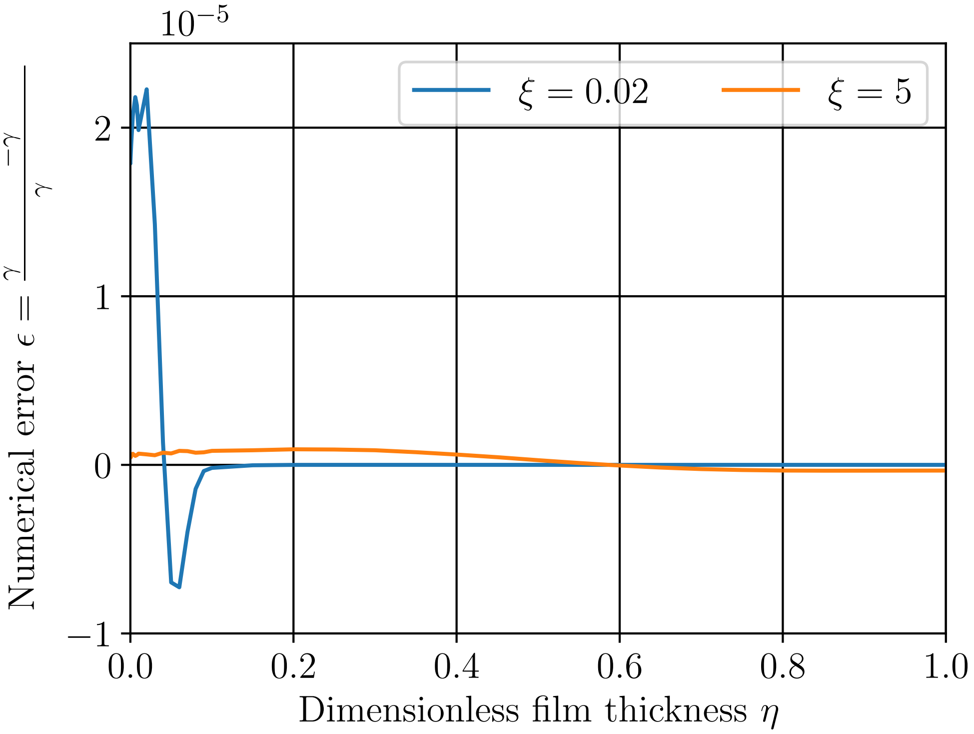

Figure 3: Numerical error of the OCFE integration scheme for the baseline model. Error is the difference to the ground truth analytical solution [16].

4.2. Dimensionless concentration and temperature profiles

In Figure 4, the evolution of both the dimensionless concentration as well as the dimensionless temperature across the film thickness is depicted for increasing dimensionless flow coordinate values for ξ as a parameter. This dimensionless flow parameter ξ can be interpreted as the thermal entrance length of the problem, sometimes referred to as the Graetz number [12]. Roughly speaking, if $\xi < 0.1$ the film surface is unaffected by the thermal wall boundary condition and for values of $\xi > 0.1$ the thermal wall boundary condition is interfering with the film surface. Due to this evolution of the thermal boundary layers there are three basic phases of film absorption, depending on the dimensionless film flow length. In the first phase, the thermally unaffected interfacial boundary layer evolves independently from the thermal boundary condition at the wall for $\xi < 0.01$. In phase two, the thermal boundary condition strongly affects the evolution of the concentration gradient, keeping the mass absorption almost constant for the applied isothermal wall boundary condition in the range of $0.01 < \xi < 1$. In phase three the completely different nature of the two distinct cases under investigation becomes evident looking at the evolution of the dimensionless concentrations for $10 < \xi < 100$. The dimensionless absorbate concentration saturates in case of pure physical absorption at $\gamma_{eq} = 2$ but reaches a constant steady state condition between the mass flow that reacts and the mass flow that is being absorbed in case of the non-isothermal reaction models.

For the initial flow coordinate of $\xi = 0.01$, the concentration profiles are just beginning to develop, and there are almost no visible differences between the five different model results for the concentration profiles. Regarding

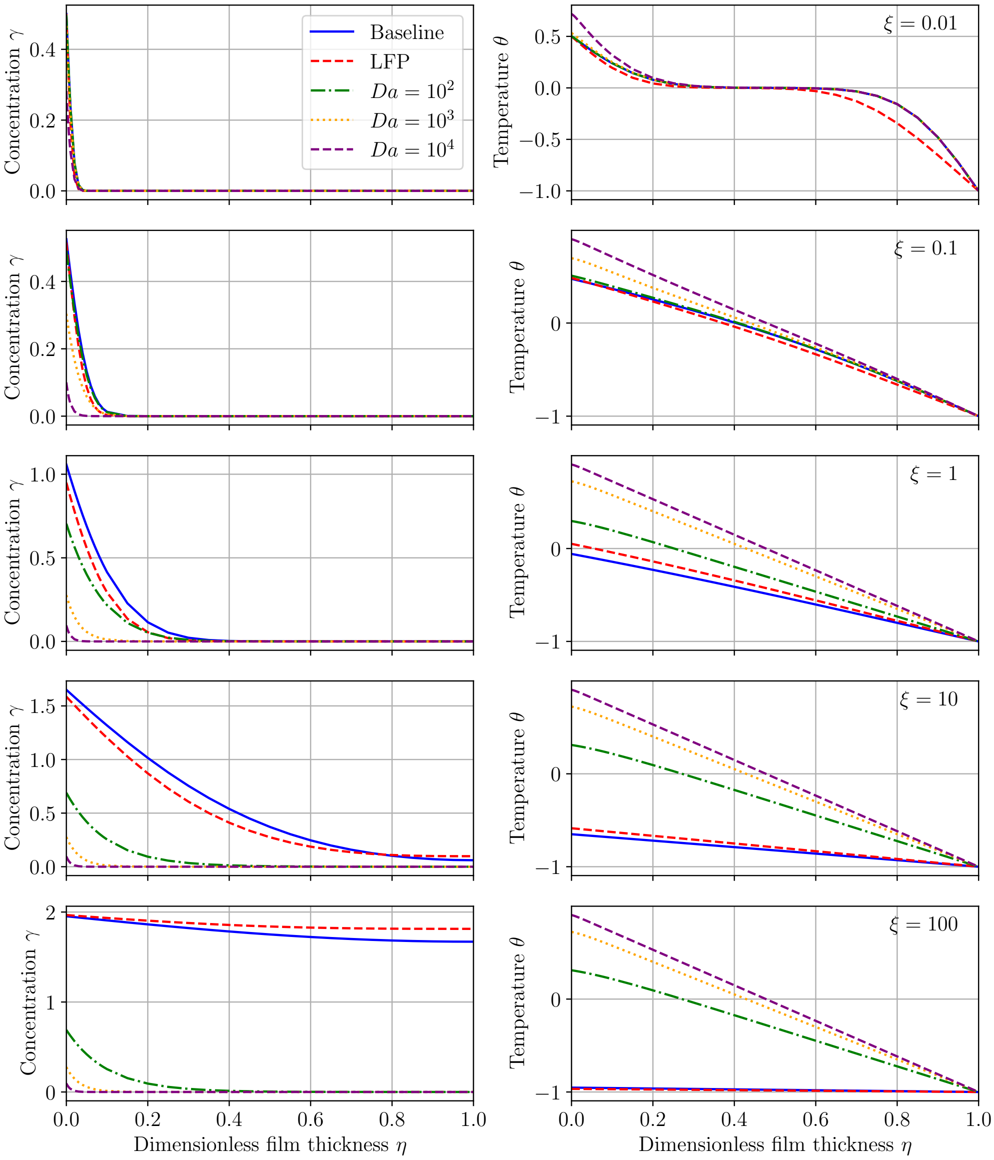

Figure 4: Dimensionless concentration and temperature profiles of Baseline model, laminar flow profile (LFP), and reactive absorption for different Da numbers. $\widetilde{St}_R = 0.1$ for all results.

the temperature profiles, however, an elevated film surface temperature can be seen for the largest Damköhler number due to the additional heat of the reaction that is released close to the surface, in addition to the heat of absorption set free at the film surface. Also, for the steady-state laminar flow profile, the temperature profile close to the wall is less steep due to the lower film velocity and hence lower convective heat flow in the transversal direction close to the wall, which in turn results in lower temperature gradients at the wall compared to all the other models.

Increasing the flow coordinate value further, the differences between the different models become more prominent. At $\xi = 1$, the temperature profile across the film thickness is fully evolved, but the slopes of the temperature gradients differ significantly between the different models, translating to different heat flows transported across the film. The highest film surface temperature corresponds to the largest Damköhler number and, hence, the largest heat flow through the film. This originates first in the highest reaction rates for $Da = 10^4$ and the additional heat of the chemical reaction that is in the same order of magnitude as the heat of absorption in this case. For the lower Damköhler numbers, the film surface temperature decreases accordingly due to lower reaction rates. Comparing the two absorption models without chemical reactions, the film temperature and its gradient of the steady-state film flow profile are higher throughout the film thickness at $\xi = 1$ compared to the baseline model, indicating a higher heat flow. The surface concentration is inversely connected to the temperature profiles through the thermodynamic equilibrium (Equation (25)). At $\xi = 1$, the lowest concentration corresponds to the highest film surface temperature for $Da = 10^4$

and the highest film concentration to the baseline model.

Further increasing the flow coordinate, the different evolutions of the concentration profiles become prominent between the pure absorption cases compared to the reactive absorption. For the cases of the purely physical absorption, the absorbate capacity within the film itself is limited, almost reaching the saturation or corresponding equilibrium concentration of $\gamma_I = 2$ for the thermal wall boundary condition throughout the film for $\xi = 100$. On the contrary, for the reactive film absorption, the concentration profiles reach a steady state approximately at $\xi \approx 1$ at the point where the absorbate consumption of the chemical reaction within the film equals the physical absorption at the film surface.

4.3. Absorption rate

The absorption rate, i.e., the mass flow of absorbate into the film, is an important quantity for sizing absorption apparatuses. We assume that all the mass absorbed by the film is transported into the film. Thus, the absorption rate is equal to the mass transport at the interface in the transverse direction, which is described by Fick's law at the interface:

$$\dot{m}_{abs} = -D\rho \frac{\partial c}{\partial y}\bigg|_I \tag{54}$$

Here, $\dot{m}_{abs}$ is the local absorbate mass flux. We define μ as the dimensionless absorbate mass flux that is given as:

$$\mu = \frac{\dot{m}_{abs}\delta}{D\rho(c_{eq} - c_0)} = -\frac{\partial \gamma}{\partial \eta}\bigg|_I \tag{55}$$

As μ is equal to the negative dimensionless concentration gradient at the interface, we can compute the values via the OCFE approximation. Here,

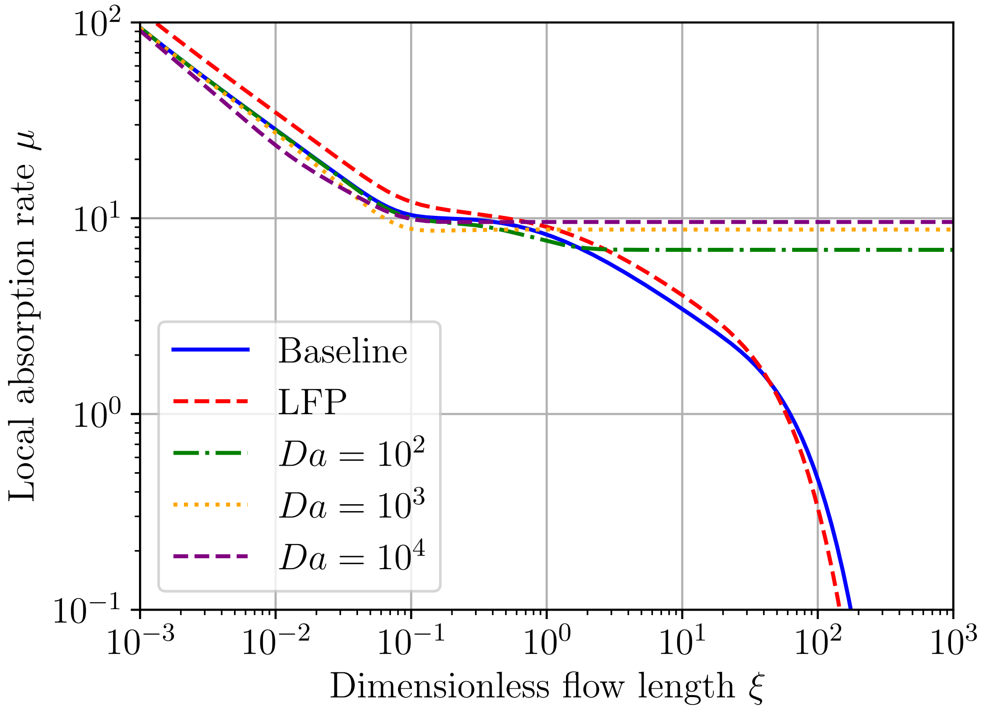

Figure 5: Local absorption rate (Equation (55)) of Baseline model, laminar flow profile (LFP), and reactive absorption for different Da numbers. $\widetilde{St}_R = 0.1$ for all results.

we simply evaluate Equation (45) for the first finite element, i.e., for $\eta = 0$. To obtain the medium absorption rate as a function of the film length, we integrate over ξ:

$$\bar{\mu} = \frac{1}{\xi} \int_0^{\xi} \mu \, d\xi \tag{56}$$

The evolution of the local absorption rate is depicted in Figure 5. Clearly, the local absorption rate of the steady state model is the highest for film flow length $\xi < 0.1$ due to the highest interfacial film velocity and, hence, increased longitudinal absorbate transfer within the film. Increased Damköhler number and the increased interfacial temperature lead to decreasing local absorption rates for the unaffected interface regarding the thermal wall boundary condition for $\xi < 0.01$. For the highest Damköhler number of $Da = 10^4$, the thermal wall boundary condition starts to affect the interfacial concentration gradient observable by a slightly less negative slope for $0.01 < \xi < 0.1$. Then, for a film flow length of $0.1 < \xi < 1$, the temperature profile is fully developed, actively cooling the film surface. This cooling of the interface leads to a drop in interfacial temperature and an increase in interfacial absorbate concentration according to the thermodynamic equilibrium. However, the increase in interfacial absorbate concentration stops the decrease in the local concentration gradient, keeping them almost constant for all models at different levels. Also, the onset of the thermally induced stop or slowdown of the decrease of the concentration gradient varies for the models. It seems to happen at lower ξ values for larger Damköhler numbers due to higher film temperatures and increased heat conduction.

In the third phase for $\xi > 1$, the evolution of the different models varies significantly due to the different nature of the problems. For the purely physical absorption models, the film saturates in absorbate and will inevitably reach a final equilibrium state corresponding to the thermal wall boundary condition. The models with chemical reactions reach steady states with constant mass absorption rates, which equal the mass flow rates that are consumed by the chemical reactions for the different Damköhler numbers, respectively.

Figure 6 depicts the averaged interfacial gradient according to Equation (56), i.e., the average absorbed mass flow. The average absorbed mass flow rate for the steady state flow profile is higher than for the plug flow

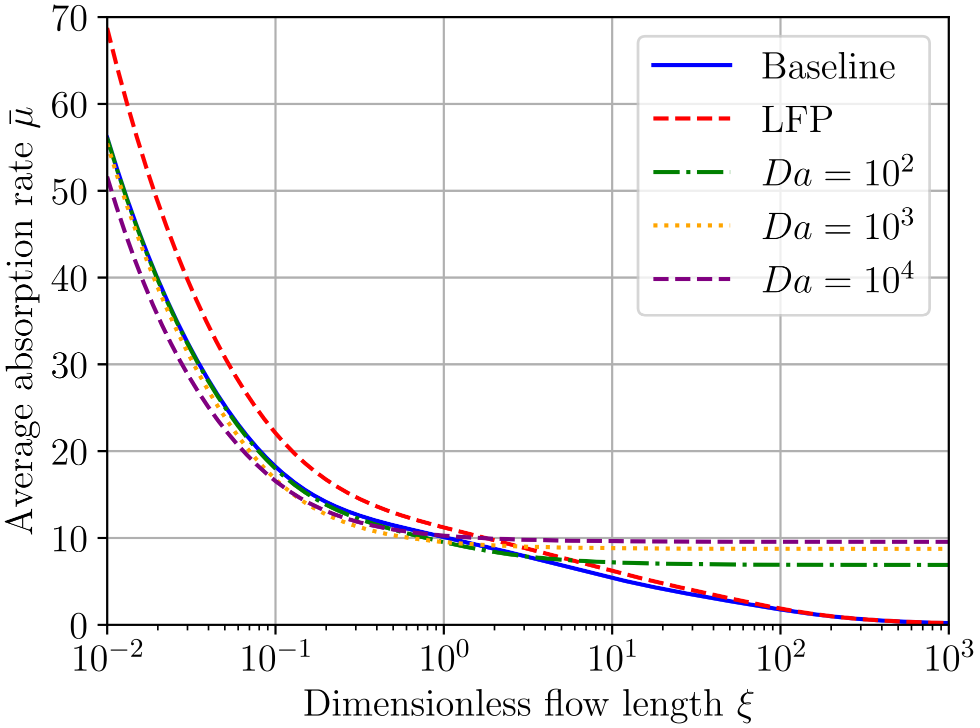

Figure 6: Average absorption rate (Equation (56)) of Baseline model, laminar flow profile (LFP), and reactive absorption for different Da numbers. $\widetilde{St}_R = 0.1$ for all results.

solution, as already presented by [3]. All the models with chemical reactions start at lower average mass flow rates due to the elevated film temperatures for the interfacial boundary layer, unaffected by the wall cooling. As soon as the thermal wall boundary layer affects the surface for $\xi > 0.1$, the average mass flow rates reach their constant level when the absorbed mass flow equals the mass consumed by the chemical reaction.

In order to better emphasize the differences between the absorbed mass flows at the surface for the different models, we introduce a local mass absorption enhancement factor:

$$\beta_i(\xi) = \frac{\mu_i(\xi)}{\mu_{bl}(\xi)}. \tag{57}$$

The enhancement factor compares the dimensionless local concentration gradient μ_i of each model to the corresponding local concentration gradient of the baseline model μ_{bl} at the interface as a function of ξ. According to Equation 55, the concentration surface gradients are directly proportional to the absorbed mass flow.

Figure 7 shows the evolution of this enhancement factor. Note that the figure only shows four plots for the laminar flow profile (LFP) and the three reactive absorption models, as the results are relative to the results of the baseline model.

In the first absorption phase for $\xi < 0.01$, the enhancement factor for the laminar film profile is larger than one only since the interfacial film velocity is increased compared to the baseline model with the average uniform film velocity. This result aligns with our observations in Figure 5. For the reactive absorption case, the local interfacial concentration gradients are lower and even decrease compared to the baseline model since the reaction heat is accumulated in the thermally unaffected interfacial film flow. This effect increases with increasing reaction rates, hence, larger Damköhler numbers.

The evolution of the enhancement factor varies significantly as soon as the cooled wall affects the interface in phase two of the absorption process, which happens at different values for the film flow lengths depending on the intensity of the heat conduction from both sides, the wall, and the interface. In the case of the stationary laminar film profile, the enhancement factor drops from 1.2 to 1.1 when the wall boundary hits the interface for $0.08 < \xi < 0.5$.

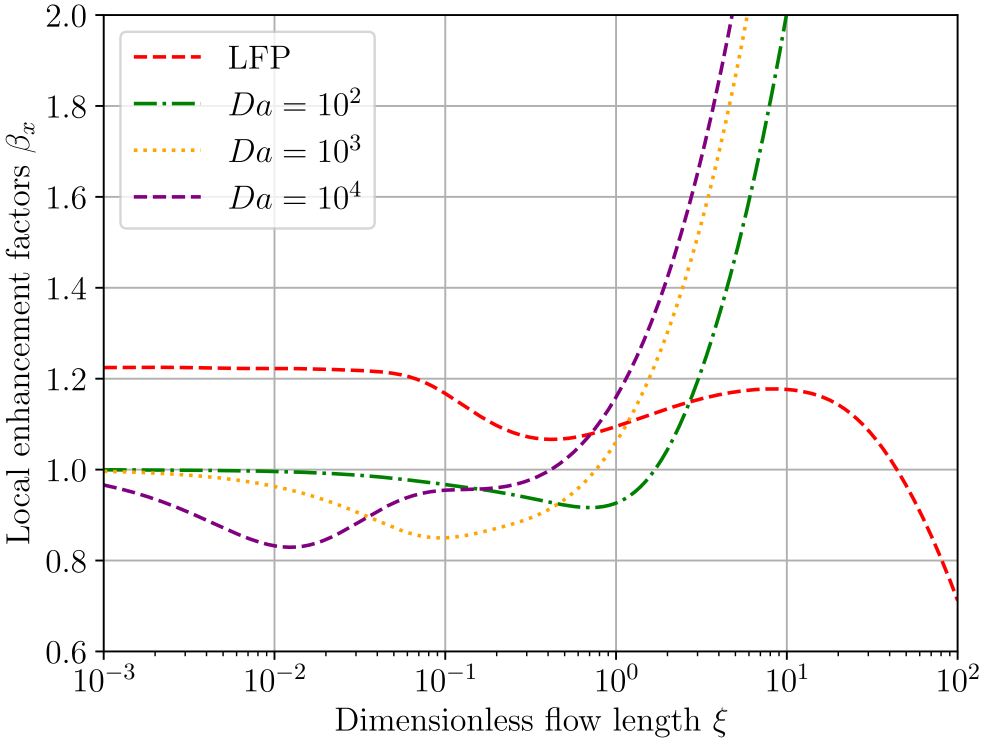

Figure 7: Local mass absorption enhancement factor (Equation (57)) for laminar flow profile (LFP) and reactive absorption for different Da numbers. $\widetilde{St}_R = 0.1$ for all results.

The drop corresponds to a hindered and delayed evolution of the thermal boundary layer from the wall to the slow-flowing fluid for the laminar flow profile compared to the baseline. As soon as the thermal boundary is evolved, the enhancement factor increases before dropping below 1 for large $\xi > 50$ due to mass conservation.

All the cases of reactive absorption are not enhanced in phase one of the absorption for the unaffected interface boundary since the heat of reaction ($\widetilde{St}_R = 0.1$) and, hence, elevated film temperatures decrease the interfacial concentration gradients compared to the baseline. The higher the Damöhler number, the stronger the enhancement factor drops below 1. The larger interfacial temperatures, however, lead to an early onset of the cooling effect for the highest Damköhler number of $Da = 10^4$ at $\xi \approx 0.01$, leading to an increase of β until also the baseline model is affected by the cooled wall, which then leads to an almost constant evolution of β. At around $\xi = 0.5$, the enhancement factor increases drastically due to the decrease of the baseline concentration gradient due to the saturation of absorbate, compared to an already almost constantly high concentration gradient for the reactive absorption case with $Da = 10^4$. A similar evolution can be observed for the models with lower Damköhler numbers, but due to the lower heat of reaction, the onset of the cooling effect is shifted to a larger film flow length.

The influence of various heats of reaction ($\widetilde{St}_R$) and reaction rates (Da) is depicted in Figure 8. As a reference, the previous cases for $\widetilde{St}_R = 0.1$ and $Da = 10^3$ (yellow dotted line) and $Da = 10^4$ (purple dashed line) are depicted, which both exhibit enhancement factors below 1 for $\xi < 5$ and $\xi < 9$, respectively. The isothermal reaction cases for $\widetilde{St}_R \to \infty$ for $Da = 10^3$

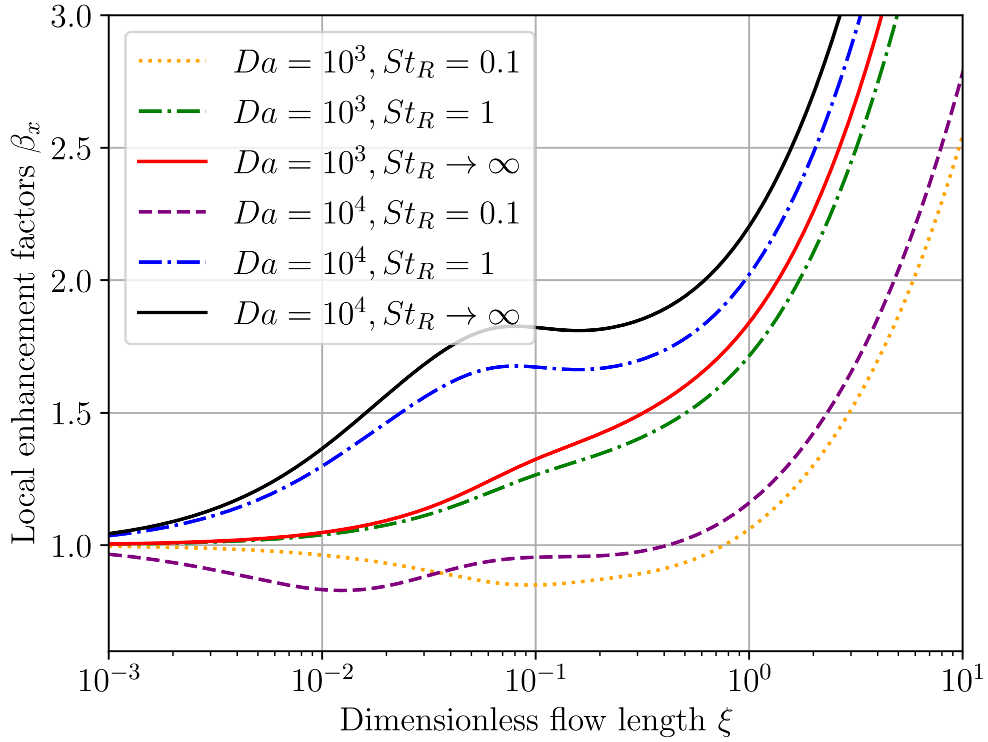

Figure 8: Local mass absorption enhancement factor (Equation (57)) for reactive absorption. Impact of reaction heat ($\widetilde{St}_R$) and reaction rate (Da). Note that $\widetilde{St}_R \to \infty$ indicates isothermal reaction, i.e., no reaction heat.

(solid red line) and $Da = 10^4$ (solid black line) lead to enhancement factors above 1 for all ξ since the concentration gradient at the surface is elevated by the chemical reaction without any negative thermal effect by the chemical reaction. The larger the reaction rates, the larger the Damköhler numbers, the higher the enhancement factors. For a small heat of reaction $\widetilde{St}_R = 1$, the two given reaction rates $Da = 10^3$ (green dash-dotted line) and $Da = 10^4$ (blue dash-dotted line) exhibit slightly lower enhancement factors than the respective isothermal reaction cases for the same Damköhler numbers. It seems as if there is a combination of the dimensionless quantities for which the local enhancement factor compared to the physical absorption drops below 1 for small and medium dimensionless flow length $\xi < 5$. According to Equation (31), the following ratio of dimensionless numbers seems to have a significant influence on the temperature evolution within the film:

$$\frac{Da}{\widetilde{St}_R \; Le} = \frac{k \cdot \delta^2 \cdot \Delta h_R}{c_p \cdot \alpha} \cdot \underbrace{\frac{(c_{eq} - c_0)}{(T_{eq} - T_0)}}_{=\frac{1}{A}} \tag{58}$$

This dimensionless group of parameters can be interpreted as the amount of reaction heat in the numerator and the heat capacity and the thermal diffusivity in the denominator, indicating the local temperature increase due to the chemical reaction. The parameter 'A' represents the slope of a linearized boiling line as a function of the absorbate mass fraction as introduced in Figure 7 of our previous work [34]. The larger this dimensionless group, the higher the local film temperature compared to the purely physical absorption. As can be seen from Figure 8, there seems to be a critical value for this number for which the local dimensionless concentration gradient drops below the value of that of the physical absorption, despite the absorbate being consumed by the reaction. Typically, the negative thermal influence on the absorption is neglected, and hence the state of the art leads to larger enhancement factors than 1 for all chemical reaction cases [35].

5. Conclusion

We present a numerical integration scheme for the coupled heat and mass transfer in falling film absorption. We discretize the coupled PDE system using OCFE in the direction of the dimensionless film thickness and obtain a DAE system, which we solve efficiently by implementation in *Modelica* and using the integration software in *Dymola*. The proposed scheme efficiently solves different falling film models. We use the numerical scheme to solve the well-established models of purely physical film flow absorption with uniform and laminar velocity film profiles. Additionally, we model and solve three different cases of reactive film flow absorption with high reaction enthalpy.

Reactive absorption yields some noteworthy results. In particular, the heat of reaction initially decreases the absorption rates compared to the purely physical absorption case until the cooled wall enhances the absorbed mass flow for the chemical reaction cases. For cases without reaction heat, there is an increase in the absorption rate compared to the purely physical absorption, which is usually assumed in literature and considered as state of the art. The observation of a lower absorption rate resulting from reaction heat extends the current state-of-the-art presented in textbooks on reactive absorption in falling films.

There are a number of additional models of falling film absorption that we did not discuss in this work. Future work should consider the effects of unidirectional diffusion, increasing film thickness, and wavy films. Further applications of our scheme include the computation of absorption rates for process design and the necessary additional cooling power for absorption and reaction heat.

Appendix A. Numerical Solution using OCFE

The first derivatives are:

$$\mathcal{A}_1(z, h_k) = 6z(z-1) \tag{A.1a}$$

$$\mathcal{A}_2(z, h_k) = (1-3z)(1-z)h_k \tag{A.1b}$$

$$\mathcal{A}_3(z, h_k) = 6z(1-z) \tag{A.1c}$$

$$\mathcal{A}_4(z, h_k) = z(3z-2)h_k \tag{A.1d}$$

The second derivatives are given by:

$$\mathcal{B}_1(z, h_k) = 6(2z-1) \tag{A.2a}$$

$$\mathcal{B}_2(z, h_k) = (6z-4)h_k \tag{A.2b}$$

$$\mathcal{B}_3(z, h_k) = 6(1-2z) \tag{A.2c}$$

$$\mathcal{B}_4(z, h_k) = (6z-2)h_k \tag{A.2d}$$

Table A.4 lists the values of the cubic Hermite polynomials and their first and second derivatives.

Table A.4: Values of the cubic Hermite polynomials and their first and second derivatives.

	$u_1 = 0$	$u_2 = \frac{3-\sqrt{3}}{6}$	$u_3 = \frac{3+\sqrt{3}}{6}$	$u_4 = 1$
$\mathcal{H}_1$	1	0.88490	0.11510	0
$\mathcal{H}_2/h_k$	0	0.13145	0.03522	0
$\mathcal{H}_3$	0	0.11510	0.88490	1
$\mathcal{H}_4/h_k$	0	-0.03522	-0.13145	0
$\mathcal{A}_1$	0	-1	-1	0
$\mathcal{A}_2/h_k$	1	0.28868	-0.28868	0
$\mathcal{A}_3$	0	1	1	0
$\mathcal{A}_4/h_k$	0	-0.28868	0.28868	1
$\mathcal{B}_1$	-6	-3.46410	3.46410	6
$\mathcal{B}_2/h_k$	-4	-2.73205	0.73205	2
$\mathcal{B}_3$	6	3.46410	-3.46410	-6
$\mathcal{B}_4/h_k$	-2	-0.73205	2.73205	4

Appendix A.1. Implementation in Modelica

Terms in the Modelica Model:

$$\int_0^{\eta_w=1} \gamma \, d\eta = I_g \tag{A.3}$$

$$\frac{1}{Le} \int_0^{\xi} \mu \, d\xi = I_{mL} \tag{A.4}$$

$$\Rightarrow \mu / Le = der(I_{mL}) \tag{A.5}$$

$$\frac{Da}{Le} \int_0^{\xi} \int_0^{\eta_w=1} \gamma \, d\eta \, d\xi = rxn \tag{A.6}$$

$$\Rightarrow der(rxn) = (Da/Le) I_g \tag{A.7}$$

$$I_{mL} = I_g + rxn \tag{A.8}$$

The general OCFE algorithm is implemented in a partial model that serves as the base for our PDE system. This partial model defines initial conditions for the interior collocation points (differential variables) and enforces continuity constraints, Equation (41) and (42), on the border elements (algebraic variables). This partial model is realized in two instances, which constitute the discretized PDEs for θ and γ and approximate the solutions to Equations (40) and (43). Figure A.9 shows a simplified Unified Modeling Language (UML) class diagram to visualize the relationship between the models.

Our implementation of this process in Dymola takes advantage of Modelica's object-oriented nature, allowing Dymola to combine submodels into a single main model efficiently, see Figure A.10. Here, we have separate models for each balance equation and the boundary conditions. The boundary conditions at the wall and interface are defined in separate Modelica models and then connected to the PDE models via connectors. The boundary conditions

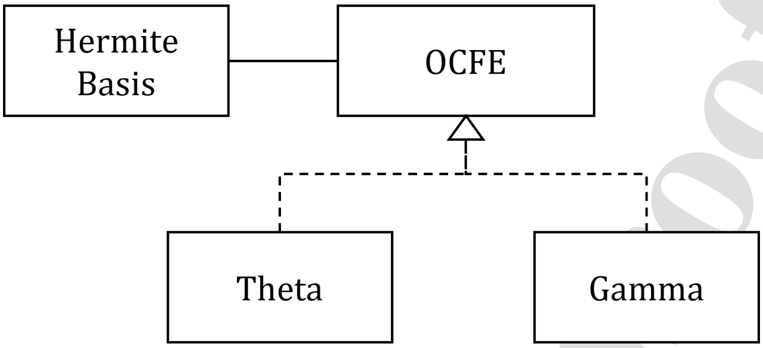

Figure A.9: Simplified UML class diagram of the partial models.

are automatically assigned to the first and last points on the entire finite elements grid (dark grey elements in Figure 2). This compartmentalization makes it easier for us to change the boundary conditions.

Appendix B. Mass balance analysis

We compute an integral mass balance over the film in a steady state to check the numerical results' physical plausibility. The general total mass balance for all possible models from Section 2 reads:

$$0 = \dot{M}_0 - \dot{M}(x) + \dot{M}_{abs} - \dot{R} \tag{B.1}$$

Here, $\dot{M}_0$ is the inlet mass flow, $\dot{M}(x)$ is the total absorbent mass flow at film length x, $\dot{M}_{abs}$ is the total absorption mass flow, and $\dot{R}$ is the total reaction

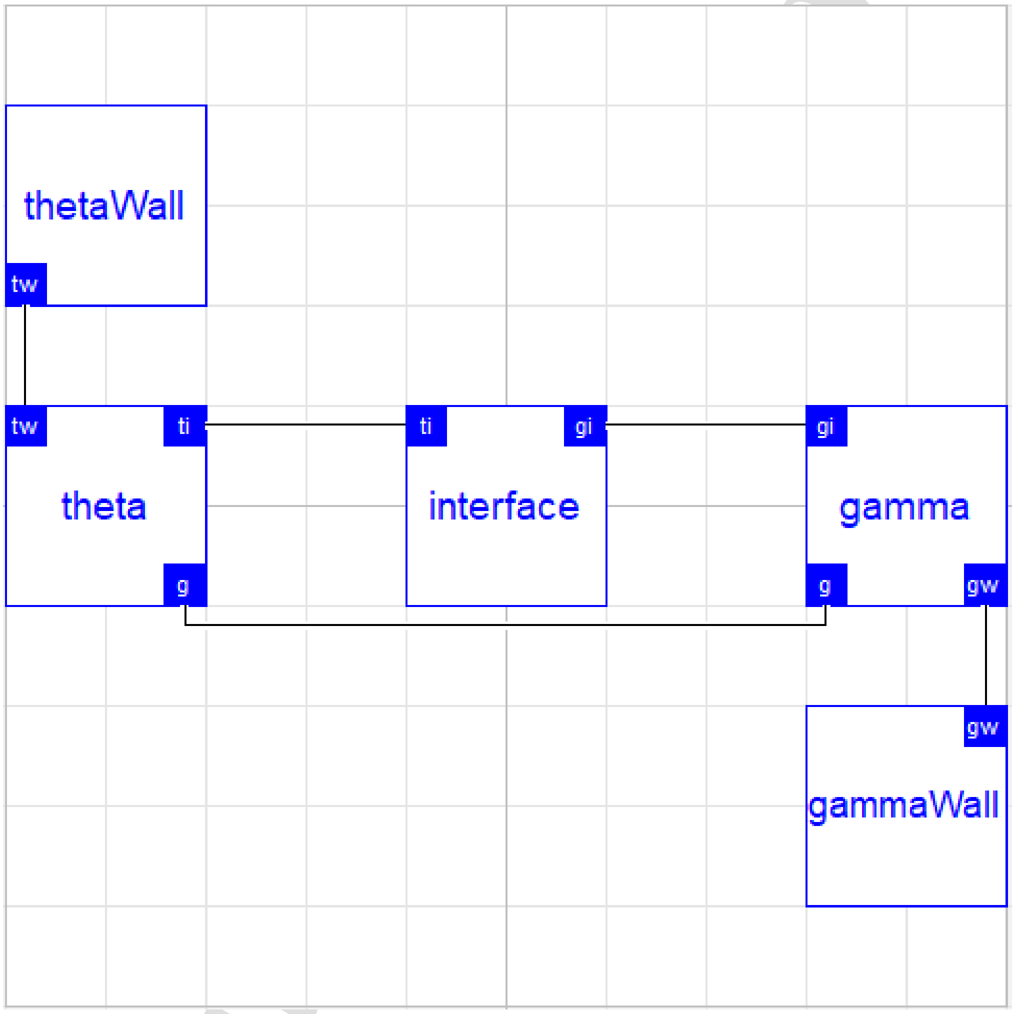

Figure A.10: Aggregation in Dymola, here for the third model (first-order reaction).

rate.

$$\dot{M}_{abs}(x) = \int_0^x \dot{m}_{abs} B dx \tag{B.2}$$

$$\dot{M}_0 = \int_0^\delta u_x(y) \rho B c_0 \, dy \tag{B.3}$$

$$\dot{M}(x) = \int_0^\delta u_x(y) \rho B c(x,y) \, dy \tag{B.4}$$

$$\dot{R}(x) = \int_0^x \int_0^\delta k c(x,y) \rho B \, dy dx \tag{B.5}$$

Using the dimensionless numbers, the three total mass balances for the baseline, laminar flow, and first-order reaction read as follows, respectively:

$$\frac{1}{Le} \int_0^\xi \mu \, d\xi = \int_0^{\eta_w=1} \gamma \, d\eta \tag{B.6}$$

$$\frac{1}{Le} \int_0^\xi \mu \, d\xi = \int_0^{\eta_w=1} \frac{3}{2}(1-\eta^2) \gamma \, d\eta \tag{B.7}$$

$$\frac{1}{Le} \int_0^\xi \mu \, d\xi = \int_0^{\eta_w=1} \gamma \, d\eta + \frac{Da}{Le} \int_0^\xi \int_0^{\eta_w=1} \gamma \, d\eta \, d\xi \tag{B.8}$$

The dimensionless absorption rate μ is given by Equation (55). The integrals are calculated using the Gaussian Quadrature method presented in Section 3.2 and the DAE reformulation in Section 3.3, respectively.

Figure B.11 shows the results of this integration, confirming the validity of the applied numerical results since the physical models reach their physical absorbate maximum of $\gamma = 2$ for the applied wall temperature of $\Theta_W = -1$. All models with reactive absorption have no final value and infinitely absorb mass, which then reacts in the film.

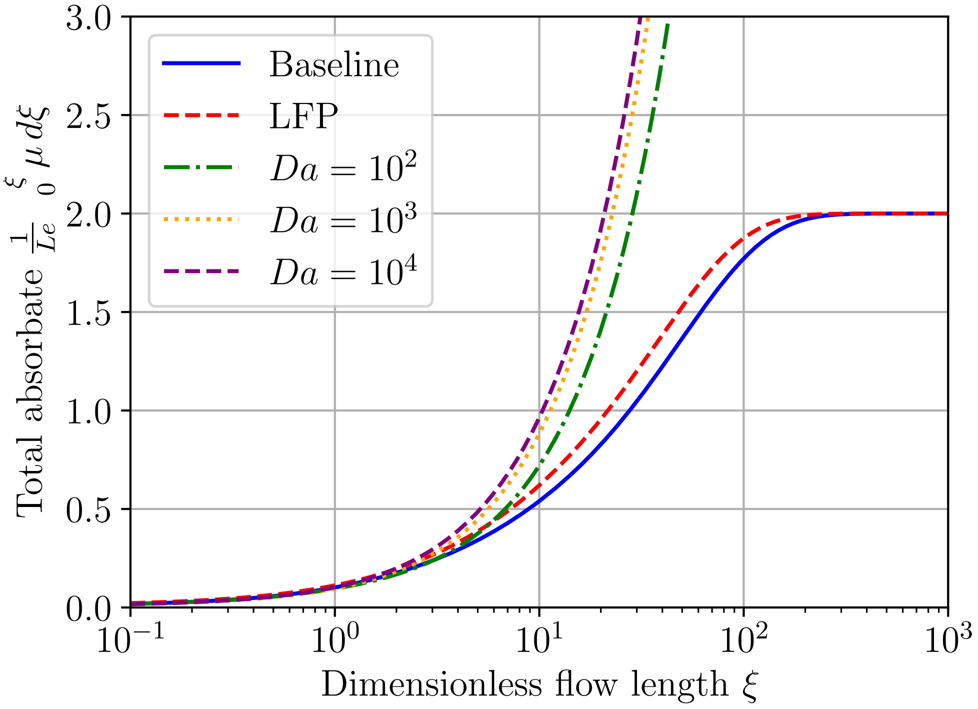

Figure B.11: Integral mass flow rates of the different models. The acronyms are laminar flow profile (LFP) and reactive absorption (RA).

Nomenclature

Variables

Variable	Description	Unit
u	Film velocity	m s^{-1}
$\bar{u}$	Average film velocity	m s^{-1}
x	Flow coordinate	m
y	Film thickness coordinate	m
c	Absorbate mass fraction	kg kg^{-1}
ρ	Density	kg m^{-3}
λ	Thermal conductivity	W m^{-1} K^{-1}
α	Thermal diffusivity	m^2 s^{-1}
D	Mass diffusivity	m^2 s^{-1}
c_p	Specific heat capacity	kJ kg^{-1} K^{-1}
T	Film temperature	K
A, B	Constants	K
Δh	Specific enthalpy difference	kJ kg^{-1}
k	Reaction constant	s^{-1}
$\dot{r}$	Reaction rate	kg m^{-3} s^{-1}
$\dot{q}$	Heat of reaction	kW m^{-3}
δ	Film thickness	m
z	Local variable	
h	Finite element length	
$\dot{m}_{abs}$	Absorbate mass flux	kg m^{-2} s^{-1}
$\dot{M}$	Mass flow rate	kg s^{-1}

Abbreviations

Abbreviation	Meaning
NE	Number of elements
DAE	Differential Algebraic Equations
PDE	Partial Differential Equations
OCFE	Orthogonal Collocation on Finite Elements
LFP	Laminar Flow Profile

Indices

Indices	Description
I	Interface
A	Absorption
W	Wall
0	Inlet value
max	Maximum value
x	in x direction
R	Reaction
k	Finite element index
l	Collocation index
analytical	Analytical solution
OCFE	Solution from OCFE scheme
ref	reference
eq	equilibrium

Dimensionless Numbers

Name	Symbol	Definition
Damköhler	Da	$\frac{k\delta^2}{D}$
Lewis	Le	$\frac{\alpha}{D}$
Stefan absorption	$\widetilde{St}_A$	$\frac{c_p(T_{eq}-T_0)}{\Delta h_A(c_{eq}-c_0)}$
Stefan reaction	$\widetilde{St}_R$	$\frac{c_p(T_{eq}-T_0)}{\Delta h_R(c_{eq}-c_0)}$

Acknowledgements

E.C. gratefully acknowledges the financial support of the Kopernikus project SynErgie 3 by the Federal Ministry of Research, Technology, and Space (BMFTR) and the project supervision by the project management organization Projektträger Jülich (PTJ).

Data Availability

The *Modelica* code and other research data will be made available upon reasonable request.

Author Contribution CRediT

E.C.: Conceptualization, Formal analysis, Investigation, Methodology, Supervision, Writing – original draft, revision; R.R.: Formal analysis, Investigation, Methodology, Software, Validation, Visualization, Writing – original draft T.M.: Formal analysis, Literature review Investigation, Validation, Writing – original draft, revision;

References

[1] J. D. Killion, S. Garimella, A critical review of models of coupled heat and mass transfer in falling-film absorption, International Journal of Refrigeration 24 (8) (2001) 755–797.

[2] N. I. Grigor'eva, V. E. Nakoryakov, Exact solution of combined heat- and mass-transfer problem during film absorption, Journal of Engineering Physics 33 (5) (1977) 1349–1353. `doi:10.1007/bf00860913`.
URL `http://dx.doi.org/10.1007/BF00860913`

[3] G. Grossman, Simultaneous heat and mass transfer in film absorption under laminar flow, International Journal of Heat and Mass Transfer 26 (3) (1983) 357–371.

[4] N. Brauner, D. M. Maron, H. Meyerson, Coupled heat condensation and mass absorption with comparable concentrations of absorbate and absorbent, International Journal of Heat and Mass Transfer 32 (10) (1989) 1897 – 1906. `doi:https://doi.org/10.1016/0017-9310(89)90159-2`.

[5] N. Brauner, Non-isothermal vapour absorption into falling film, International Journal of Heat and Mass Transfer 34 (3) (1991) 767 – 784. `doi:https://doi.org/10.1016/0017-9310(91)90124-W`.

[6] J. Andberg, Absorption of vapours into liquid films flowing over cooled horizontal tubes, Ph.D. thesis, University of Texas (1986).

[7] V. Patnaik, Combined heat and mass transfer in wavy-film absorption, Ph.D. thesis, Pennsylvania State University (1994).

[8] V. Patnaik, H. Perez-Blanco, A study of absorption enhancement by wavy film flows, International Journal of Heat and Fluid Flow 17 (1) (1996) 71–77. `doi:https://doi.org/10.1016/0142-727X(95)00076-3`.
URL `https://www.sciencedirect.com/science/article/pii/0142727X95000763`

[9] E. Garcia-Rivera, J. Castro, J. Farnos, A. Oliva, Numerical and experimental investigation of a vertical libr falling film absorber considering wave regimes and in presence of mist flow, International Journal of Thermal Sciences 109 (2016) 342–361. `doi:https://doi.org/10.1016/j.ijthermalsci.2016.05.029`.
URL `https://www.sciencedirect.com/science/article/pii/S1290072916306767`

[10] R. Yang, Heat and mass transfer in laminar wavy film absorption with the presence of non-absorbable gases, Ph.D. thesis, Arizona State University (1987).

[11] E. Garcia-Rivera, J. Castro, J. Farnos, C. Oliet, Numerical and experimental study of absorption of h2o vapor in wavy falling film of libr aqueous solution in vertical tubes and in presence of non-absorbables, International Journal of Refrigeration 100 (2019) 184–195. `doi:https://doi.org/10.1016/j.ijrefrig.2019.01.022`.
URL `https://www.sciencedirect.com/science/article/pii/S0140700719300362`

[12] H. Wassenaar, R., Simultaneous Heat and Mass Transfer in a Horizontal Tube Absorber, Ph.D. thesis, Delft University of Technology (1994).

[13] V. Subramaniam, S. Chandrasekaran, S. Garimella, A 2-d numerical analysis of heat and mass transfer in lithium bromide-water falling films and droplets, International Journal of Heat and Mass Transfer 177 (2021) 121518. `doi:https://doi.org/10.1016/j.ijheatmasstransfer.2021.121518`.
URL `https://www.sciencedirect.com/science/article/pii/S0017931021006219`

[14] M. Mittermaier, P. Schulze, F. Ziegler, A numerical model for combined heat and mass transfer in a laminar liquid falling film with simplified hydrodynamics, International Journal of Heat and Mass Transfer 70 (2014) 990 – 1002. `doi:https://doi.org/10.1016/j.ijheatmasstransfer.2013.11.075`.

[15] J. Castro, A. Oliva, C. Perez-Segarra, C. Oliet, Modelling of the heat exchangers of a small capacity, hot water driven, air-cooled h2o-libr absorption cooling machine, International Journal of Refrigeration 31 (1) (2008) 75–86. `doi:https://doi.org/10.1016/j.ijrefrig.2007.05.019`.
URL `https://www.sciencedirect.com/science/article/pii/S0140700707001570`

[16] T. Meyer, Analytical solution for combined heat and mass transfer in laminar falling film absorption with uniform film velocity-diabatic wall

boundary, International Journal of Heat and Mass Transfer 80 (2015) 802–811.

[17] M. Ashouri, M. Bahrami, Heat and mass transfer in laminar falling film absorption: A compact analytical model, International Journal of Heat and Mass Transfer 188 (2022) 122598. `doi:10.1016/j.ijheatmasstransfer.2022.122598`.
URL `http://dx.doi.org/10.1016/j.ijheatmasstransfer.2022.122598`

[18] V. Russo, A. Milicia, M. Di Serio, R. Tesser, Falling film reactor modelling for sulfonation reactions, Chemical Engineering Journal 377 (2019) 120464. `doi:10.1016/j.cej.2018.11.162`.
URL `http://dx.doi.org/10.1016/j.cej.2018.11.162`

[19] N. A. Gómez Mendoza, I. Dobrosz-Gómez, M. A. Gómez García, Modeling and simulation of an industrial falling film reactor using the method of lines with adaptive mesh. study case: Industrial sulfonation of tridecylbenzene, Computers & Chemical Engineering 68 (2014) 233–241. `doi:10.1016/j.compchemeng.2014.05.023`.
URL `http://dx.doi.org/10.1016/j.compchemeng.2014.05.023`

[20] P. Nielsen, J. Villadsen, Absorption with exothermic reaction in a falling film column, Chemical Engineering Science 38 (9) (1983) 1439–1454. `doi:10.1016/0009-2509(83)80079-7`.
URL `http://dx.doi.org/10.1016/0009-2509(83)80079-7`

[21] B. Finlayson, Nonlinear Analysis in Chemical Engineering, Chemical

Engineering, McGraw-Hill International Book Company, 1980.
URL `https://books.google.de/books?id=uMRTAAAAMAAJ`

[22] B. A. Finlayson, Orthogonal collocation on finite elements—progress and potential, Mathematics and Computers in Simulation 22 (1) (1980) 11–17. `doi:https://doi.org/10.1016/0378-4754(80)90097-X`.
URL `https://www.sciencedirect.com/science/article/pii/037847548090097X`

[23] L. T. Biegler, Nonlinear Programming: Concepts, Algorithms, and Applications to Chemical Processes, Society for Industrial and Applied Mathematics, 2010. `arXiv:https://epubs.siam.org/doi/pdf/10.1137/1.9780898719383`, `doi:10.1137/1.9780898719383`.
URL `https://epubs.siam.org/doi/abs/10.1137/1.9780898719383`

[24] T. Meyer, Analytical solution for combined heat and mass transfer in laminar falling film absorption with uniform film velocity - isothermal and adiabatic wall, International Journal of Refrigeration 48 (08 2014).

[25] T. Meyer, F. Ziegler, Analytical solution for combined heat and mass transfer in laminar falling film absorption using first type boundary conditions at the interface, International Journal of Heat and Mass Transfer 73 (2014) 141–151. `doi:https://doi.org/10.1016/j.ijheatmasstransfer.2014.01.074`.
URL `https://www.sciencedirect.com/science/article/pii/S001793101400115X`

[26] H. Löwer, Thermodynamische und physikalische Eigenschaften der

wässrigen Lithiumbromid-Lösung, Ph.D. thesis, Technische Hochschule Karlsruhe (1960).

[27] R. Bird, W. Stewart, E. Lightfoot, Transport Phenomena, J. Wiley, 2002.
URL `https://books.google.de/books?id=wYnRQwAACAAJ`

[28] G. Carey, B. A. Finlayson, Orthogonal collocation on finite elements, Chemical Engineering Science 30 (5) (1975) 587–596. `doi:https://doi.org/10.1016/0009-2509(75)80031-5`.
URL `https://www.sciencedirect.com/science/article/pii/0009250975800315`

[29] M. Abramowitz, Handbook of mathematical functions with formulas, Graphs, and Mathematical Tables (1965).

[30] I. A. Ganaie, S. Arora, V. K. Kukreja, Cubic hermite collocation method for solving boundary value problems with dirichlet, neumann, and robin conditions, International Journal of Engineering Mathematics 2014 (2014) 1–8. `doi:10.1155/2014/365209`.
URL `http://dx.doi.org/10.1155/2014/365209`

[31] G. Bärwolff, Numerik für Ingenieure, Physiker und Informatiker, Vol. 1, Springer, 2007.

[32] T. Meyer, Analytische lösung des gekoppelten wärme- und stofftransportproblems bei der absorption im laminaren rieselfilm, Ph.D. thesis, Technische Universität Berlin (2016).

[33] A. Beutler, Stoff- und Wärmeübergang bei der Rieselfilmabsorption am horizontalen Rohr, Ph.D. thesis, Technische Universität München (1997).

[34] T. Meyer, F. Ziegler, Analytical solution for combined heat and mass transfer in laminar falling film absorption using first type boundary conditions at the interface, International Journal of Heat and Mass Transfer 73 (2014) 141–151. `doi:https://doi.org/10.1016/j.ijheatmasstransfer.2014.01.074`. URL `https://www.sciencedirect.com/science/article/pii/S001793101400115X`

[35] M. Kraume, Grundlagen der Transportprozesse, Springer Berlin Heidelberg, Berlin, Heidelberg, 2020, pp. 3–75.

- Solution to coupled heat and mass transport using orthogonal collocation on finite elements
- Solution of first-order reaction diffusion model
- Reduced absorbate mass flow resulting from excess heat of reaction

Declaration of Interest Statement

☒ The authors declare that they have no known competing financial interests or personal relationships that could have appeared to influence the work reported in this paper.

☐ The author is an Editorial Board Member/Editor-in-Chief/Associate Editor/Guest Editor for this journal and was not involved in the editorial review or the decision to publish this article.

☐ The authors declare the following financial interests/personal relationships which may be considered as potential competing interests:

Eike Cramer